Far-reaching transient motions after Mojave earthquakes require broad mantle flow beneath a strong crust

Andrew M. Freed[1], Roland Bürgmann[2], and Thomas Herring[3]

[1]Department of Earth and Atmospheric Sciences, Purdue University, West Lafayette, Indiana, USA

[2]Department of Earth and Planetary Science, University of California Berkeley, Berkeley, California, USA

[3]Department of Earth, Atmospheric, and Planetary Sciences, Massachusetts Institute of Technology, Cambridge, Massachusetts, USA

Geophysical Research Letters, In Press, 2007

Abstract

Geodetically observed postseismic surface displacements in the 7 years following the 1999 Hector Mine earthquake demonstrate a previously unrecognized broad pattern of transient deformation throughout southern California and into Nevada, more than 200 km from the epicenter. Unlike previous postseismic observations in which trade-offs between postseismic mechanisms and the depth of flow lead to non-unique solutions, this deformation pattern can only be explained by viscoelastic flow in a region of the mantle 100s of km wide and below a depth of 40 km. This result enables two robust conclusions regarding the nature of lithospheric strength in this region to be reached: the mantle is weaker than the lower crust, and flow occurs over a wide region of mantle as opposed to within a narrow shear zone beneath the fault.

Introduction

The variation of strength with depth of continental lithosphere is much debated. Depending on the composition and water content of the lower crust, warm temperatures may lead to a weak viscously deforming layer sandwiched between strong upper-crustal and upper-mantle layers; i.e. a "jelly sandwich" structure [e.g., Chen and Molnar, 1983]. Hotter temperatures in the mantle combined with a higher water content could, however, cause the upper mantle to be weaker than the lower crust; i.e. a "crème brûlée" structure [Jackson, 2002; Burov and Watts, 2006]. It also continues to be a question of much debate if continental deformation at depth occurs along discrete, strain-weakened shear zones or is distributed in viscously deforming lower crust and lithospheric mantle. Because of the difficulty to directly determine viscoelastic strength and the degree of localization of deformation in the lower crust and upper mantle, there is no consensus on which region contributes most to the strength of the lithosphere and how this may vary with tectonic regime, crustal age or other factors.

A useful approach for inferring the strength of the lithosphere is to utilize earthquakes as large rock deformation experiments where coseismic stress changes induce a variety of postseismic responses, including afterslip, poroelastic rebound, and viscoelastic relaxation. Each of these mechanisms is capable of inducing observable postseismic surface deformation that can constrain numerical models to help understand the rheological properties of the lithosphere. Given the limited spatial and temporal resolution of postseismic observations, however, it has proven difficult to sort out the relative contributions of each mechanism, let alone to determine how viscosity varies as a function of depth. Consider the interpretation of postseismic deformation following the 1992 M7.3 Landers earthquake in the Mojave Desert. Studies have inferred only afterslip [Shen et al., 1994], only viscoelastic relaxation in the lower crust [Deng et al., 1998]; viscoelastic relaxation predominately in the upper mantle [Pollitz et al., 2000; Freed and Bürgmann, 2004], a combination of poroelastic rebound and afterslip [Peltzer et al., 1998; Fialko, 2004a], or a combination of poroelastic rebound and viscoelastic relaxation in the lower crust [Masterlark and Wang, 2002]. The various conclusions of these studies were influenced by the use of different data sets and modeling approaches, though it is unlikely that consensus would have been achieved with more comprehensive analyses, as the resolution of the post-Landers deformation remains a limiting factor.

The Landers earthquake was followed soon after by the nearby 1999 M7.1 Hector Mine quake (Figure 1). As the Hector Mine earthquake was of similar magnitude and sense of slip as Landers, and perturbed the same crust and mantle, one would expect a similar postseismic response. Unlike the Landers quake, however, postseismic deformation following the Hector Mine quake was recorded at an extensive array of continuous GPS stations that span a very broad region of southern California and into Nevada (more than 200 km from the epicenter). This first of a kind far-field view (over 4 rupture lengths) of a postseismic deformation field following a strike-slip earthquake, allows us to much more uniquely determine the mechanism responsible for this broad deformation pattern.

Observational Constraints and Modeling Approach

We rely on daily time-series from continuously operating GPS sites, most of which are part of the SCIGN network that became operational between 1996 and 2001. The time-series are used to estimate horizontal and vertical components of linear interseismic displacement rates, coseismic offsets, and a logarithmically decaying function that represents the postseismic signal (see Supporting Online Material). Seven years of cumulative transient deformation resolves a broad postseismic response (Figure 1, black arrows) to the 1999 M7.1 Hector Mine earthquake, as well as continued deformation from the nearby 1992 M7.3 Landers earthquake. The postseismic response reaches the vicinity of Yucca Mountain, Nevada, more than 200 km from the Hector Mine epicenter (Figure 1, inset).

To understanding the mechanism responsible for this deformation pattern we use a 3-D viscoelastic finite element model of the Mojave region that incorporates both rupture surfaces (Supplementary Figure S2a). We use the inferred coseismic slip distribution of Fialko [2004b] for the Landers earthquake, and that of Simons et al. [2002] for the Hector Mine earthquake, as well as the same layered elastic structure (Supplementary Figures S2b and S2c). For every candidate rheology investigated (except poroelastic rebound for which we calculate an immediate cumulative response), we first simulate the Landers rupture, allow the rheology to respond to these stress changes for 7 years, then simulate the Hector Mine rupture and allow the rheology to respond for another 7 years. Calculated cumulative postseismic model displacements over this latter 7-year period are compared to those observed to test each rheology.

Results

We first consider models with a layered viscoelastic structure and seek to understand the depth of flow required to explain both far-field (i.e., in the region of Yucca Mountain; inset of Figure 1) and mid-field (remaining stations in Figure 1) surface displacements. Since shallow mechanisms, such as afterslip and poroelastic rebound [Jacobs et al., 2002, Fialko, 2004a] contribute to near-field deformation (within 30 km), we do not consider near-field displacements (Supplementary Figure S3) in best-fit calculations. In an initial sensitivity study, we allow viscoelastic flow to occur in only one narrow depth interval at a time, and solve for the viscosity required at each interval to best fit the observations based on a weighted sum of squared residuals (WSSR; Figure 2a). We find that viscoelastic relaxation in the lower crust (20-28 km depth) or uppermost mantle (28-40 km depth) leads to significant misfit, especially for far-field motions, compared to viscoelastic flow below a depth of 40 km, with misfit minimized between the depths of 40-56 km.

The misfit induced by viscoelastic flow in the lower crust or uppermost mantle is large because flow in these depths leads to a wavelength of surface deformation that is shorter than the observed broad pattern. Considering a model of lower crustal flow (20-28 km depth) with a best-fit viscosity of 1.2×10^{18} Pa s. Figure 1 (blue arrows) shows that this model reasonably predicts mid-field displacements, but greatly underpredicts far-field displacements in the Yucca Mountain region (residual displacements are shown in Supplementary Figure S4b). In addition, deformation predicted by lower crustal flow greatly underpredicts displacements along the apex of curvature (green/black dashed line in Figure 1).

We considered a wide range of possible viscoelastic structures ranging from viscosity being uniform with depth below 20 km depth, to structures where viscosity decreases rapidly with depth (as might be expected due to increasing temperatures). Figure 2b shows a sample of tested viscosity structures along with calculated misfits. The best models (cyan and blue lines) are those where the viscosity below 40 km depth is an order of magnitude or more lower than the viscosity of mantle above and two orders of magnitude less than the viscosity of the lower crust. A model where flow occurs primarily below 63 km depth (black line) begins to introduce greater misfit, as below this depth coseismic stress changes are too small to drive significant flow. Displacements predicted by one of the best-fit models (blue line in Figure 2b), are shown in Figure 1 (red arrows; residual displacements are shown in Supplementary Figure S4a). It is particularly impressive how well this upper mantle flow model predicts the displacements in the area of Yucca Mountain (even the rotation of azimuth between northern and southern stations), while also matching the trend of deformation throughout southern California. It is worth noting that the best-fit model does not require consideration of lateral variations in viscosity structure despite the fact that the region encompasses several tectonic provinces. This may indicate that heterogeneities in crustal properties are not mirrored by heterogeneities in the mantle beneath, perhaps because the latter is mobile. The superiority of the upper mantle flow model compared to that of flow in the lower crust is also evident with observed vertical displacements (Figure 3).

It should be noted that the viscosities shown in Figure 2 are average values over the 7 year time period that lead to the best fit with respect to the observed cumulative displacements. The Newtonian rheology used here cannot explain very rapid early postseismic displacements. Such behavior requires a rheology where effective viscosity increases with time, such as a Burgers [Pollitz, 2003] or power-law rheology [Freed and Bürgmann, 2004]. We experimented with a power-law rheology and found that though calculated postseismic displacement time-series evolve much differently from those resulting from Newtonian rheology, they produce similar surface deformation patterns (when the depth of flow is similar), and these patterns do not vary much with time.

We can also rule out significant contributions of localized afterslip below the seismogenic zone to far-field postseismic deformation. We modeled afterslip by creating 3-km-wide shear zones in the mesh that extend downward from the base of the seismogenic zone through to the bottom of the model beneath both rupture surfaces. These zones extend to the north and south several hundreds of kilometers (green/black dashed lines in Supplementary Figure S5), a likely overestimation of the lateral extent of such shear zones. The relaxation of coseismic stresses within the shear zones is controlled by a viscoelastic rheology, with all volumes outside of this zone modeled as elastic. The maximum afterslip that can occur in the lower crust associated with the release of coseismic stresses is simulated by assigning a very low viscosity (10^{17} Pa s) to the shear zone between 20 and 28 km depth, which leads to complete relaxation of this region in the 7 year time frame of the postseismic observations. This model leads to surface displacements that are not significant beyond about 50 km from the rupture surfaces (Figure S5, blue arrows).

Similarly, we can simulate the complete release of coseismic stress in a mantle shear zone below a depth of 28 km. This model leads to modest displacements in the far-field, ~20% of the displacements observed in the Yucca Mountain region (Figure S5, red arrows). Finally, we consider narrow shear zones that cut both the lower crust and mantle beneath the Landers and Hector Mine ruptures. This model leads to far-field postseismic displacement of ~22% of that observed and insignificant displacement in many mid-field locations (Figure 1, yellow arrows; residual displacements are shown in Supplementary Figure S4d). Since the magnitudes of many of the other mid-field displacements are matched by the shear zone model, adding a component of mantle flow would lead to significant overshoot at these sites. Thus, afterslip within a localized shear zone below the seismogenic crust cannot be a significant source of the observed broad postseismic deformation pattern. To further quantify this result, we considered shear zones in the mantle ranging up to 400 km width. Only when the shear zone was large enough to incorporate the area beneath the Yucca Mountain region (~300 km width) did calculated far-field displacements approach the observed magnitude. Large postseismic far-field displacements beneath the Yucca Mountain region can only be explained by broad viscoelastic flow in the mantle.

We can also rule out a significant contribution to mid- and far-field postseismic displacements from poroelastic rebound. We use the same parameterization of poroelastic rebound employed by Fialko [2004a] to explain InSAR images following the Landers earthquake, to calculate the contribution of poroelastic rebound following the Hector Mine earthquake. We find horizontal surface displacements greater than 4 mm due to poroelastic rebound to be confined to within 50 km of the Hector Mine earthquake (Supplementary Figure S3; residual displacements are shown in Supplementary Figure S4c). Figure 3c shows that significant vertical displacements predicted by the poroelastic model are also confined to very near-field regions surrounding the Hector Mine rupture. While a poroelastic model does predict uplift to the southwest, it significantly underpredicts the observed uplift that is concentrated just beyond the reach of this mechanism.

Discussion and Conclusions

Previous postseismic studies have generally concentrated on relatively near-field displacements, usually with only a few observations beyond a rupture length. Such analyses have generally been plagued by trade-offs between different postseismic mechanisms and trade-offs between the depths at which these mechanisms operate. Like the present study, previous analyses have inferred a relatively weak mantle beneath the Mojave Desert [Pollitz et al., 2000; Pollitz, 2003; Freed and Bürgmann, 2004], but those primarily near- and mid-field studies showed trade-offs with lower crustal flow. In contrast, this analysis of broad, far-field postseismic displacements observed throughout southern California and into Nevada following the Hector Mine earthquake requires a fairly unique solution; that flow be deep (below 40 km) and distributed across 100s of km. Specifically, there are no trade-offs to lower crustal flow or narrow shear zone mechanisms or poroelastic rebound to explain significant postseismic displacements observed in the Yucca Mountain region, more than 200 km from the Hector Mine epicenter.

It is important to note that the present study does not rule out the contribution of shallow afterslip and poroelastic rebound to influence postseismic displacements in the near-field, as suggested by previous analyses [e.g., Peltzer et al., 1998; Jacobs et al., 2002; Fialko, 2004a]. In fact, near-field displacements cannot be explained solely by mantle flow and require other mechanisms being active (Supplementary Figure S4a). Near-field displacements do, however, contain a component from viscoelastic flow in the upper mantle (red arrows in Supplementary Figure S3). Thus, analyses that do not take into account a contribution from viscoelastic flow in the mantle to near-field displacements [Fialko, 2004a; Perfettini and Avouac, 2007] are likely misinterpreting the postseismic observations.

Our inference of a relatively weak mantle 40 km below the Mojave Desert is consistent with seismic velocities in the region that suggest a thin (order 10 km) mantle lid overlying a relatively hot, and likely convecting, asthenosphere [Melbourne and Helmberger, 2001]. A shallow, weak mantle is also consistent with thermal models derived from seismic tomography of western North America [Goes and van der Lee, 2002] and evidence of a shallow asthenosphere inferred from Mojave Desert xenoliths [Farmer et al., 1995]. Our inferred viscosity structure of the crust and upper mantle in western Nevada is comparable to that derived from isostatic rebound patterns of Lake Lahontan shorelines (5×10^{18} Pa s mantle under a much stronger crust [Bills et al., 2007]). It is also consistent with a strong crust and thin mantle lid overlying shallow asthenosphere (in this case at 60 km depth) inferred from analysis of postseismic deformation following the 2002 Denali, Alaska earthquake [Freed et al., 2006a, 2006b]. These findings suggest that at least in some backarcs or recent backarcs, the rheology is best described as a continuously strong, though thin, lithosphere overlying a weak asthenosphere, the so-called "crème brûlée" model [Jackson, 2002; Burov and Watts, 2006]. Considering the broad region of mantle sampled by these studies, it is possible that such a model may be appropriate for much of western North America and southern Alaska [Hyndman et al., 2005; Dixon et al., 2004].

Acknowledgements

CGPS data utilized in this study was provided by the SCIGN, BARGEN, UNAVCO and the International GNSS service networks. We thank the Scripps Institution of Oceanography Orbit and Permanent Array Center (SOPAC) for making available loosely constrained GPS products that we used in generating the GPS results presented here. We thank Eric Fielding and Paul Segall for helpful reviews.

References

Bills, B. G., K. D. Adams, and S. G. Wesnousky, Viscosity structure of the crust and upper mantle in western Nevada from isostatic rebound patterns of the late Pleistocene Lake Lahontan high shoreline, J. Geophys. Res., 112, B06405, doi:10.1029/2005JB003941, 2007.

Burov, E. B. and A. B. Watts, The long-term strength of continental lithosphere: "jelly sandwich" or "crème brûlée"?, GSA Today, 16, doi: 10.1130/1052-5173(2006)016, 2006.

Chen, W-P. and P. Molnar, Focal depths of intracontinental and intraplate earthquakes and their implications for the thermal and mechanical properties of the lithosphere, J. Geophys. Res., 88, 4183–4214, 1983.

Deng, J., M. Gurnis, H. Kanamori, and E. Hauksson, Viscoelastic flow in the lower crust after the 1992 Landers, Science, 282, 1689-1692, 1998.

Dixon, J. E., T. H. Dixon, D. R. Bell, and R. Malservisi, Lateral variation in upper mantle viscosity: role of water, Earth Planet. Sci. Lett., 222, 451-467, 2004.

Farmer, G. L., A. F. Glazner, H. G. Wilshire, J. L. Wooden, W. J. Pickthorn, and M. Katz, Origin of late Cenozoic basalts at the Cima volcanic field, Mojave Desert, California. J. Geophys. Res., 100, 8399-8415, 1995.

Fialko, Y., Evidence of fluid-filled upper crust from observations of postseismic deformation due to the 1992 Mw7.3 Landers earthquake, J. Geophys. Res., 109, B08401, doi:10.1029/2004JB002985, 2004a.

Fialko, Y., Probing the mechanical properties of seismically active crust with space geodesy: Study of the coseismic deformation due to the 1992 M w 7.3 Landers (southern California) earthquake, J. Geophys. Res., 109, B03307, doi:10.1029/2003JB002756, 2004b.

Freed, A. M. and R. Bürgmann, Evidence of power-law flow in the Mojave Desert mantle, Nature, 430, 548-551, 2004.

Freed, A. M., R. Bürgmann, E. Calais, J. Freymueller, and S. Hreinsdóttir, Implications of Deformation Following the 2002 Denali, Alaska Earthquake for Postseismic Relaxation Processes and Lithospheric Rheology, J. Geophys. Res., 111, B01401, doi:10.1029/2005JB003894, 2006a.

Freed, A. M., R. Bürgmann, E. Calais, J. Freymueller, Stress-dependent power-law flow in the upper mantle following the 2002 Denali, Alaska, earthquake, Earth Planet. Sci. Lett., 252, 481-489, 2006b.

Goes, S., and S van der Lee, Thermal structure of the North American uppermost mantle inferred from seismic tomography, J. Geophys. Res., 107, 2000JB000049, 2002.

Herring, T. A., MATLAB Tools for viewing GPS velocities and time-series, GPS Solutions, 7, 194-199, DIO 10.1007/s10291-003-0068-0, 2003.

Hyndman, R. D., C. A. Currie, and S. P. Mazzotti, Subduction zone backarcs, mobile belts, and orogenic heat, GSA Today, 15, doi: 10:1130/1052-5173, 2005.

Jackson, J., Strength of the continental lithosphere: Time to abandon the jelly sandwich?, GSA Today, 12, 4-10, doi: 10.1130/1052-5173(2002)012<0004:SOTCLT>2.0.CO, 2002.

Jacobs, A., D. Sandwell, Y. Fialko, and L. Sichoix, The 1999 (M_w 7.1) Hector Mine, California, Earthquake: Near-Field Postseismic Deformation from ERS Interferometry, Bull. Seismol. Soc. Am., 92, 1433-1442, 2002.

Masterlark, T. and H. F. Wang, Transient stress-coupling between the 1992 Landers and 1999 Hector Mine, California, earthquakes, Bull. Seismol. Soc. Am., 92, 1470-1486, 2002.

Melbourne, T., and D. Helmberger, Mantle control of plate boundary deformation, Geophys. Res. Lett., 28, 4003-4006, 2001.

Peltzer G, P. Rosen, F. Rogez, and K. Hudnut, Poroelastic rebound along the Landers 1992 earthquake surface rupture, J. Geophys. Res., 103, 30131-30145, 1998.

Perfettini, H., and J. Avouac, Modeling afterslip and aftershocks following the 1992 Landers Earthquake, J. Geophys. Res., doi:10.1029/2006JB004399, in press, 2007.

Pollitz, F. F., G. Peltzer, and R. Bürgmann, Mobility of continental mantle; Evidence from postseismic geodetic observations following the 1992 Landers earthquake. J. Geophys. Res., 105, 8035-8054, 2000.

Pollitz, F. F. Transient rheology of the uppermost mantle beneath the Mojave Desert, California. Earth Planet. Sci. Lett., 215, 89-104, 2003.

Shen, Z. K., D. D. Jackson, Y. J. Fend, et al., Postseismic deformation following the Landers earthquake, California, 28 June 1992, Bull. Seismol. Soc. Am., 84, 780-791, 1994.

Simons, M., Y. Fialko, L. Rivera, Coseismic Deformation from the 1999 Mw 7.1 Hector Mine, California, Earthquake as Inferred from InSAR and GPS Observations, Bull. Seismol. Soc. Am., 92, 1390–1402, 2002.

Figure Captions

Figure 1. Cumulative GPS observed postseismic horizontal surface displacements (transient component) for the 7 year period following the 1999 Hector Mine earthquake compared to those calculated by models of viscoelastic flow and afterslip within narrow shear zones. Stations within 20 km of the Landers and Hector Mine rupture surfaces have been excluded from this comparison (see Supplementary Figure S3 for near-field displacements). SAF: San Andreas

Fault. Inset: Enlargement of Yucca Mountain region. GPS errors are shown at the 95% confidence level, as computed using a correlated noise model as described in Herring [2003]. See Supplementary Table S1 for tabulated GPS data. Upper mantle viscosity structure is the blue line in Figure 2b. Lower crustal viscosity structure is the red line shown in Figure 2b. Green/black dashed line shows the apex of the curved deformation field to the southwest of the Landers rupture. Transient time-series of labeled stations are shown in Supplementary Figure S1.

Figure 2. (a) Weighted misfit as a function of the depth interval (defined by thin gray lines) at which viscoelastic flow is allowed to occur (i.e. this is a composite of results from 12 models of flow at various depths). We quantify misfit (WSSR) as $sqrt\left[(1/m)\sum(d_o - d_c)^2/\sigma^2\right]$, where d_o and d_c are the observed and calculated displacements, σ is the observational error, and m is the total number of observations. The viscosity values were tuned to match the observed displacements of "all stations" shown in Figure 1. Best-fit viscosity values decrease with depth from $4.6\text{x}10^{18}$ Pa s for the lower crustal layer from 20-24 km depth to $4.0\text{x}10^{17}$ Pa s for the region from 109-123 km depth. "Far-field only" refers to the misfit of these same models to just the far-field Yucca Mountain region stations (inset of Figure1). (b) Viscosity versus depth profile for a variety of viscoelastic flow models considered. The viscosity of all models was tuned to match the observed displacements of all stations in Figure 1. Misfits are shown for calculations based on all stations (All) and for just the far-field Yucca Mountain stations (Far-field).

Figure 3. Cumulative GPS observed postseismic vertical surface displacements (white bars show uplift, black bars show subsidence) for the 7 year period following the 1999 Hector Mine earthquake compared to those calculated (contours) by models of viscoelastic flow in (a) the upper mantle (blue line viscosity structure in Figure 2b) and (b) the lower crust (red line in Figure 2b) and (c) poroelastic rebound. GPS errors are shown at the 68% confidence level.

Stations with estimated errors greater than 5 mm in the 7-year span of the observations have been excluded from this comparison.

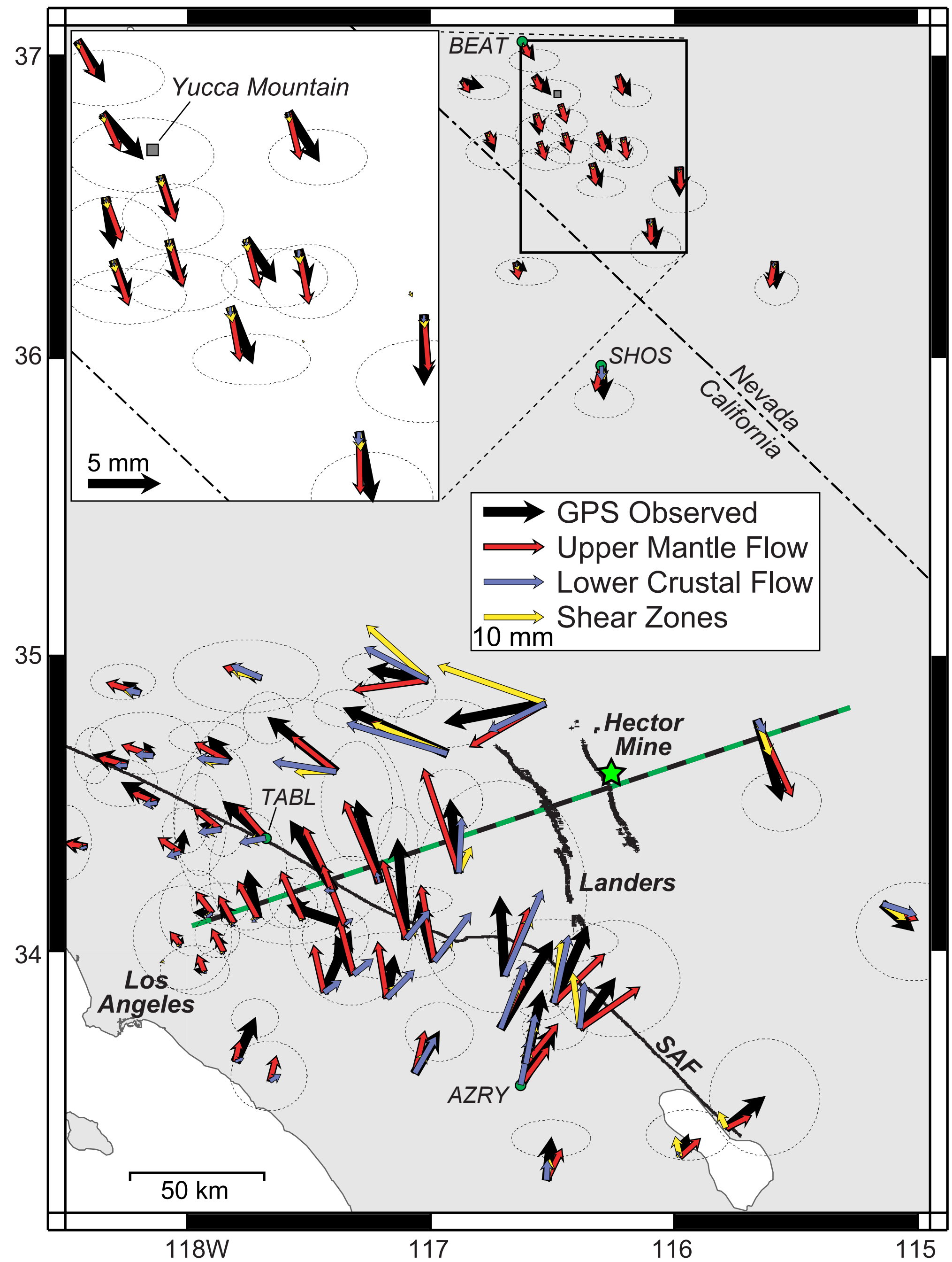
Yucca Mountain
BEAT
SHOS
Nevada
California
5 mm
GPS Observed
Upper Mantle Flow
Lower Crustal Flow
Shear Zones
10 mm
Hector Mine
TABL
Landers
Los Angeles
SAF
AZRY
50 km
37
36
35
34
118W
117
116
115

Figure 1

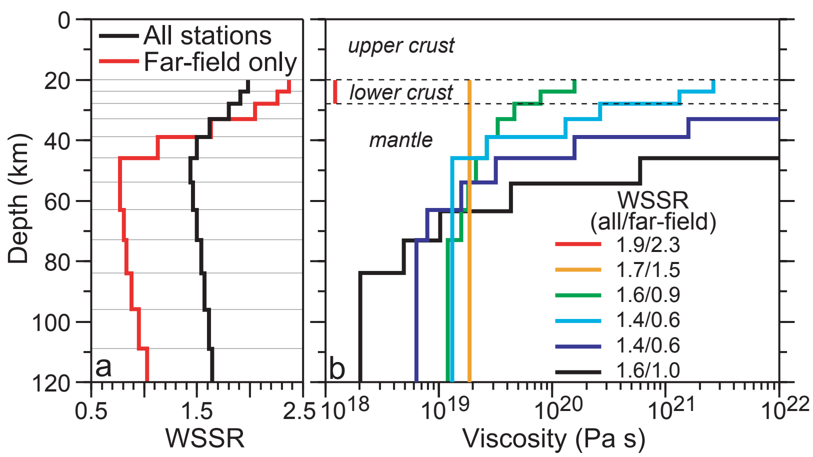

All stations
Far-field only
Depth (km)
0
20
40
60
80
100
120
a
0.5
1.5
2.5
WSSR
upper crust
lower crust
mantle
b
WSSR
(all/far-field)
1.9/2.3
1.7/1.5
1.6/0.9
1.4/0.6
1.4/0.6
1.6/1.0
10^{18}
10^{19}
10^{20}
10^{21}
10^{22}
Viscosity (Pa s)

Figure 2

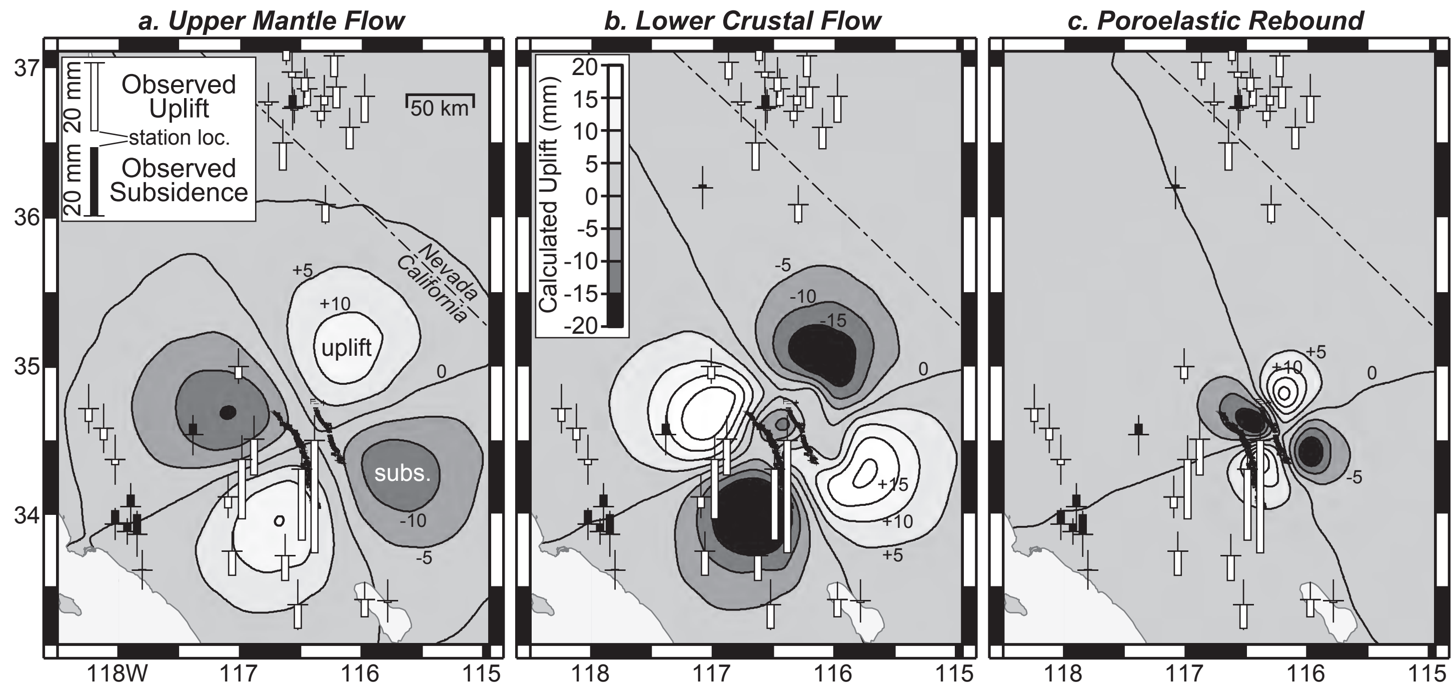

a. Upper Mantle Flow
b. Lower Crustal Flow
c. Poroelastic Rebound
Observed Uplift
20 mm
station loc.
20 mm
Observed Subsidence
50 km
Nevada
California
uplift
subs.
Calculated Uplift (mm)
37
36
35
34
118W
117
116
115
118

Figure 3

Supplementary Material: GPS Processing

GPS Time series were generated with the Gamit/Globk software package [Herring et al., 2006] from loosely constrained GPS position and orbit products (gamit h-files) generated at the SOPAC analysis center [http://sopac.ucsd.edu]. The North America Reference frame used was realized using 124 GPS sites, frame sites, distributed across North America, Greenland and Hawaii. For each day, the GPS coordinate system was aligned to the linear motion model of these frame sites through rotation, translation and scale. None of the frame sites were closer than 430 km from the epicenter of the Hector Mine earthquake.

The full time-series were used to estimate horizontal and vertical components of linear interseismic displacement rates, coseismic offsets on the day of the Hector Mine earthquake, and a decaying relaxation function starting at the day of the earthquake. The postseismic data were fit to a natural logarithmic function of the form,

$$X(t) = x_0 + \nu(t - t_m) + [C + \lambda \ln(1 + (t - t_{eq})/\tau))]\Theta(t_{eq}), \tag{1}$$

where ν is the linear rate, C the coseismic offset, $\Theta(t_{eq})$ is a Heavy-side step function at the time of the earthquake, λ is the amplitude of the logarithmic term, τ is the time constant of the logarithmic form used for all the time-series (here 10 days), and t, t_m, and t_{eq} are the time of each daily epoch, of the first epoch and of the earthquake, respectively (http://gpsweb.mit.edu/~tah/GGMatlab). Thus, the magnitude of postseismic displacements at any epoch (e.g., 7 years as chosen for the postseismic analysis) can be estimated from the optimal log-coefficients fit to the individual time-series. Examples of transient time-series in the north, east, and vertical directions are shown in Supplementary Figure S1. Tabulated GPS data is shown in Supplementary Table S1. It should be noted that, according to our finite element model results, about 1/3 of the cumulative displacements (less for near-field stations) arises from continued viscoelastic relaxation following the 1992 Landers earthquake. Displacements from two separate earthquakes can be modeled by a single logarithmic curve and a linear rate because the contribution from the Landers earthquake from 7 to 14 years after its occurrence has a slowly varying rate. As noted in the Hector Mine time-series shown in Supplementary Figure S1, very fast rate changes only occur in the first few years after the events.

We ran tests that show that the changing the time constant does affect the estimate of the log coefficients, but when the total displacement over 7 years is computed (the quantity we are comparing in this analysis), the estimated total offsets are very close (<1 mm differences for 10days compared with 100 days). If the time constant is increased to 1000 days, the fit to the initial (first year) transients degrades, though the total offset estimate is still within 2-3 mm. The uncertainty of the estimates increases with longer time constants.

Vertical GPS displacements are inherently more noisy and susceptible to non-tectonic influences. We thus restrict our comparisons (Figure 3) to stations with estimated error of less then 5 mm over the 7-year observational period.

Supplementary References

Herring, T. A., R. W. King, and S. C. McClusky, Introduction to GAMIT/GLOBK, Release 10.3. 37 pp. Mass. Instit. of Tech., Cambridge, 2006.

a.

b.

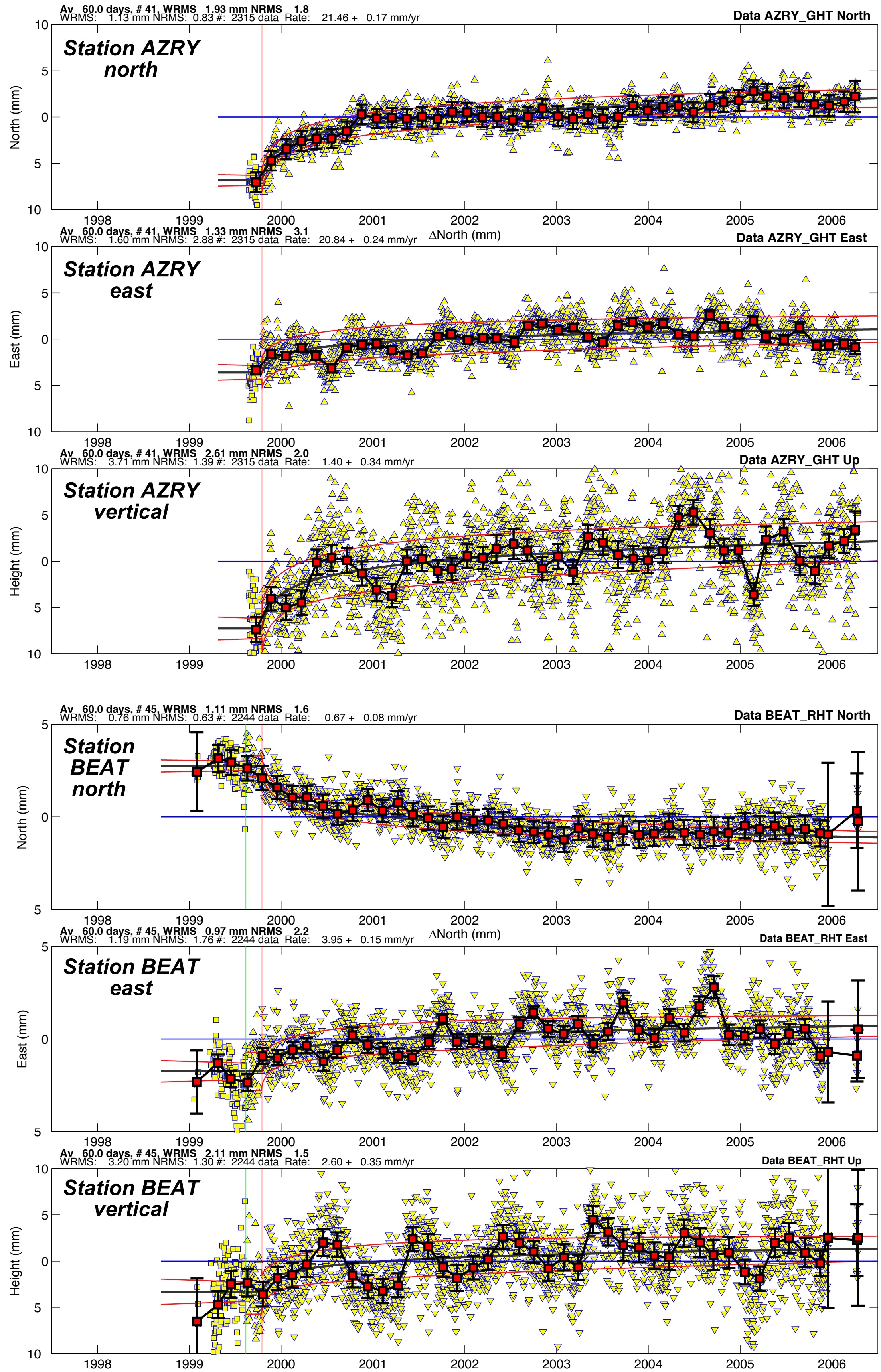

Supplementary Figure S1. Example transient GPS time-series (i.e. only the postseismic component) for four stations (a) AZRY, (b) BEAT, (c) SHOS, and (d) TABL. The secular background (linear) trend has been removed from each time-series. The location of these stations are indicated in Figure 1. Vertical red lines shows the time of the Hector Mine earthquake (vertical green lines show other estimated offsets [removed from the plot] due to either an antenna or radome change). The blue horizontal line is the arbitrary zero datum. The red squares with error bars are 60-day averages with 1-sigma error bars computed from the rms scatter within the 60-days. The thick black line that tracks through the data is the logarithmic fit, with the thin red lines on either side showing +/- 1 sigma errors.

c.

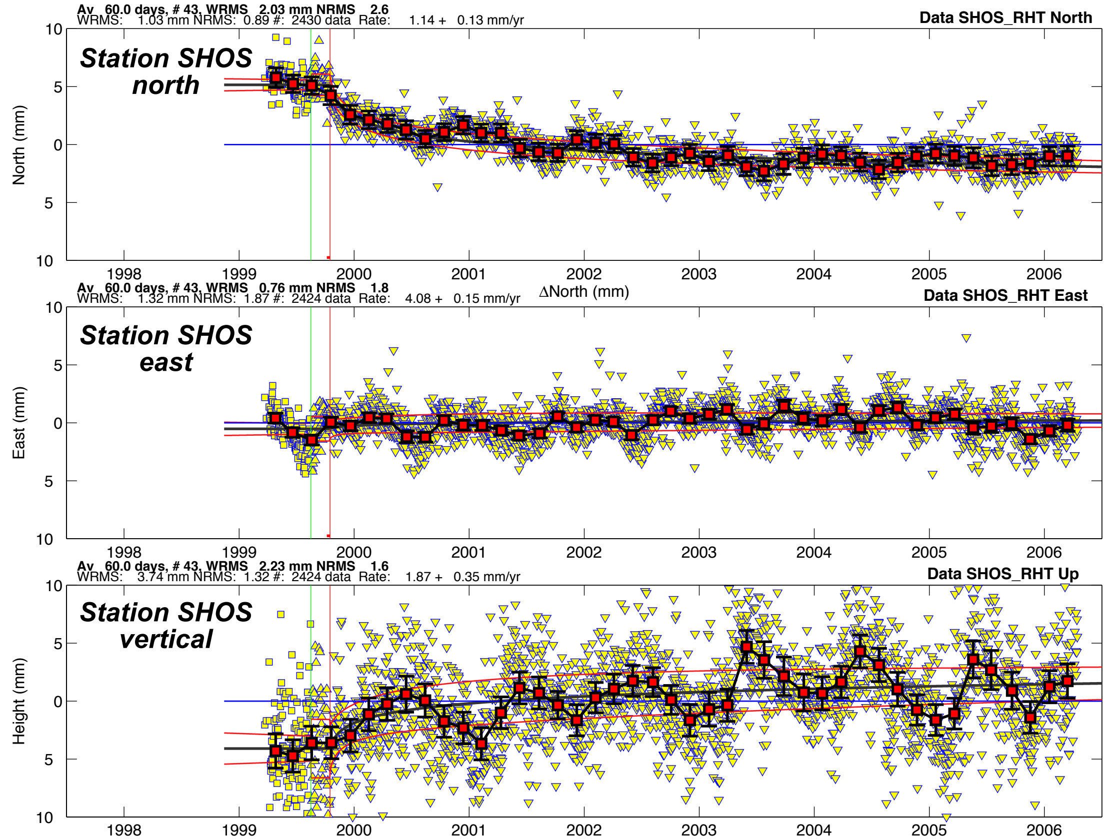

d.

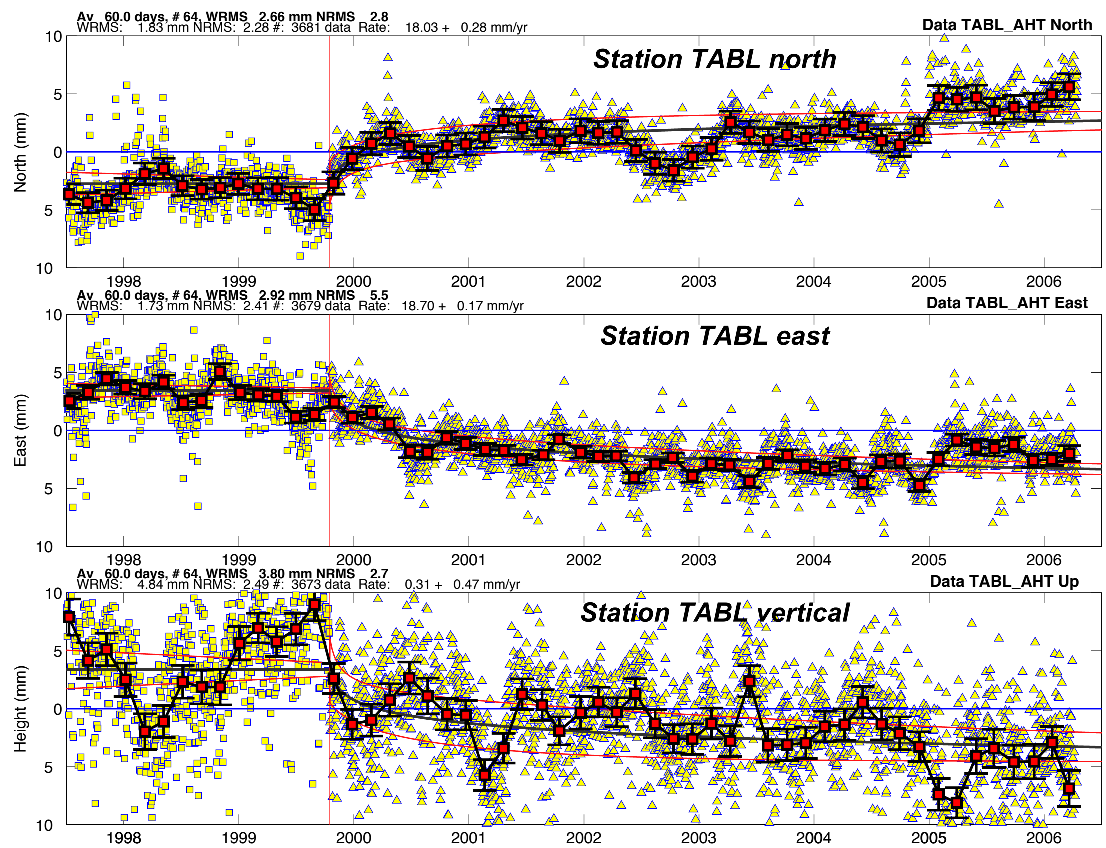

Supplementary Figure S1 (cont.)

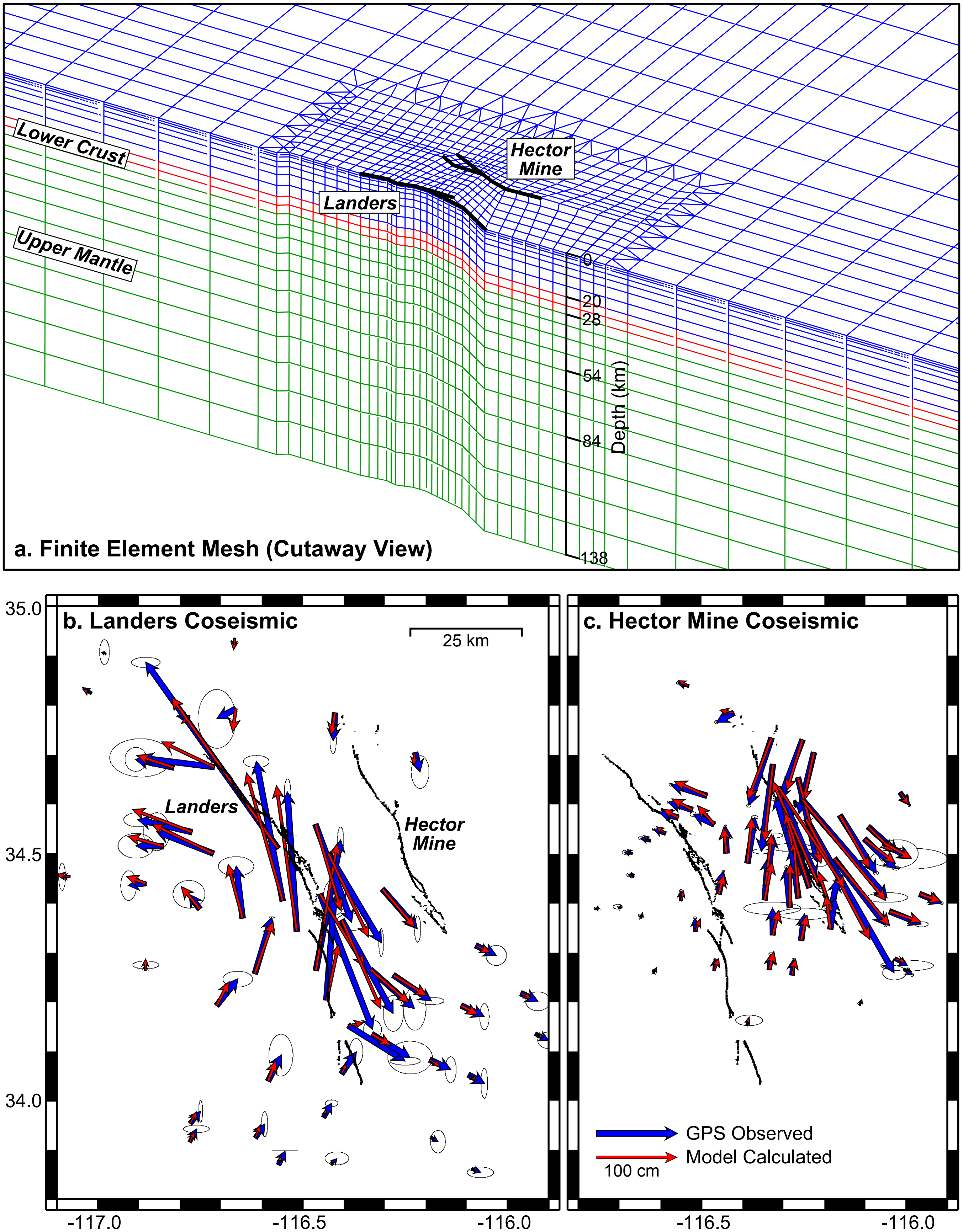

Supplementary Figure S2. (a) Cutaway view of finite element mesh along a surface through the Landers rupture surface. Surface trace of the Landers and Hector Mine rupture surfaces are shown as black lines. The mesh contains 36,000 elements and spans an area of 900 x 700 x 138 km. (b) Shows a comparison between GPS observed [Fialko, 2004b] and calculated coseismic displacements associated with the 1992 Landers earthquake. (c) Shows a comparison between GPS observed [Simons et al, 2002] and calculated coseismic displacements associated with the 1999 Hector Mine earthquake. GPS uncertainties are shown at the 95% confidence level. Black lines show the Landers and Hector Mine rupture surfaces.

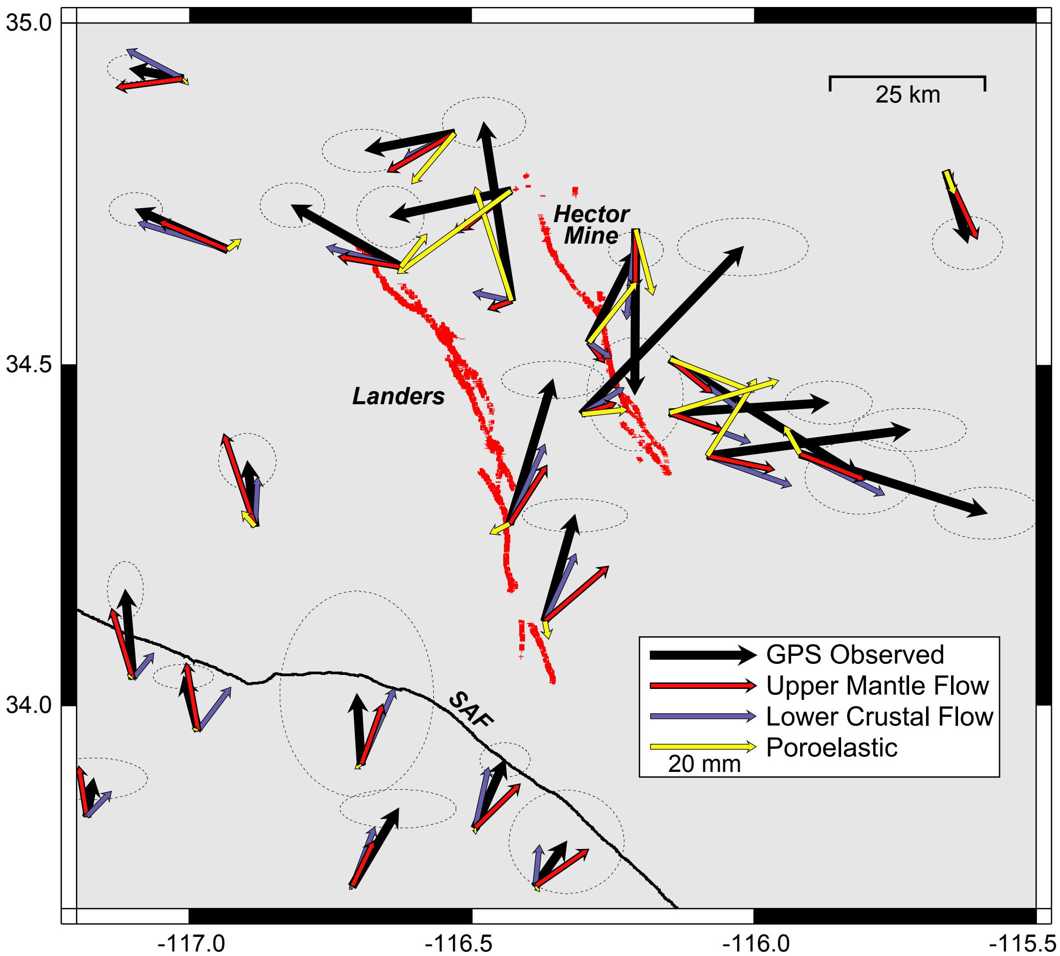

Supplementary Figure S3. Cumulative near-field GPS observed postseismic horizontal surface displacements (transient component) for the 7 year period following the 1999 Hector Mine earthquake compared to those calculated by models of viscoelastic flow and poroelastic rebound. SAF: San Andreas Fault. GPS errors are shown at the 95% confidence level, as computed using a correlated noise model as described in Herring [2003]. Upper mantle viscosity structure is the blue line in Figure 3b. Lower crustal viscosity structure is the red line shown in Figure 3b. Model results generally fail to match observed GPS displacements near the faults as these are due to multiple mechanisms, including shallow afterslip, which is not included in any of these models. Note how displacements associated with poroelastic flow (yellow arrows) are confined primarily to within 10s of km of the Hector Mine rupture surface.

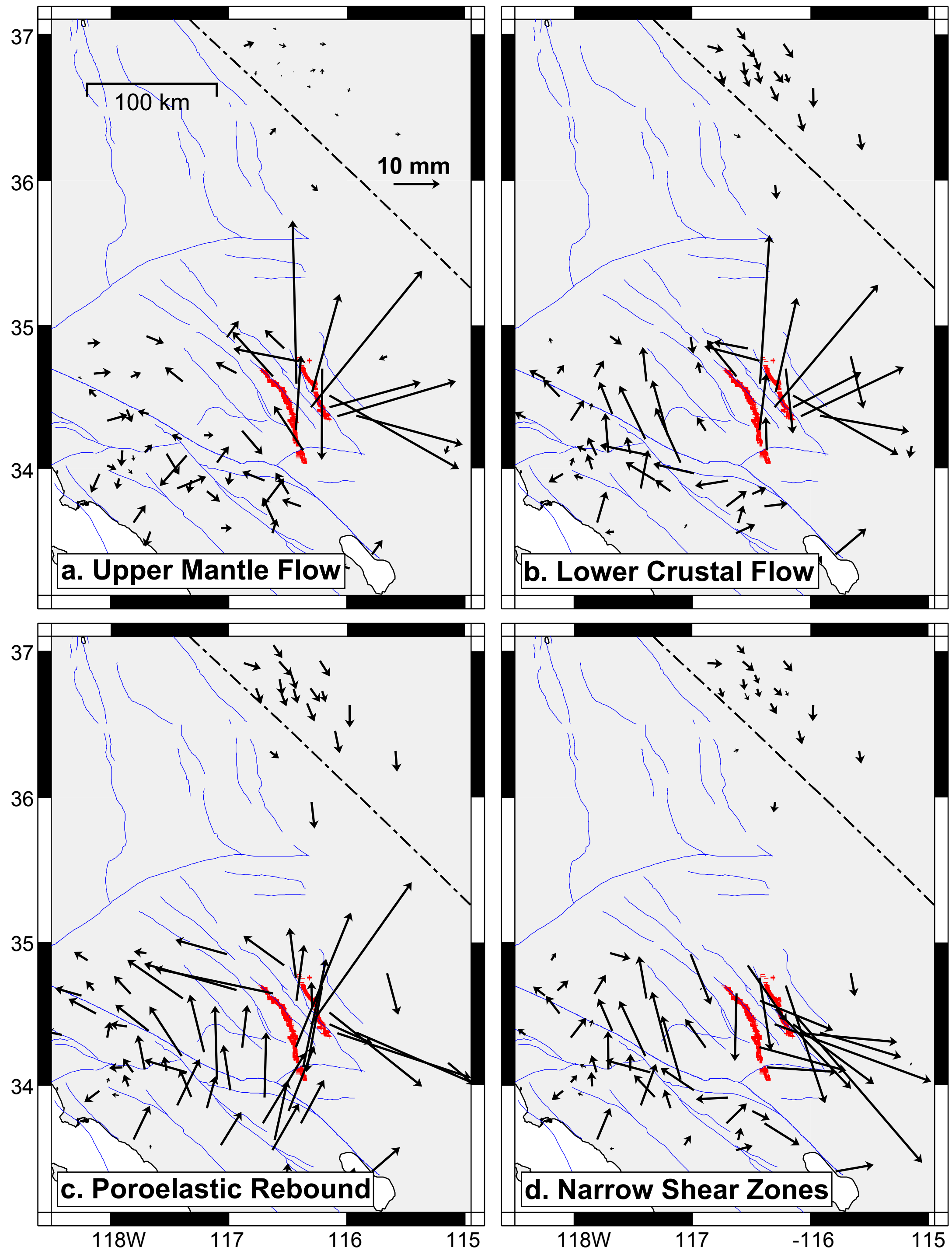

Supplementary Figure S4. Residual displacements (observed minus calculated) for models of (a) viscoelastic flow within the upper mantle (blue line in Figure 3b), (b) viscoelastic flow within the lower crust (red line in Figure 3b), (c) poroelastic rebound, and (d) within narrow 3-km-wide shear zones within the lower crust and upper mantle and extending 100s km to the north and south of the rupture region.

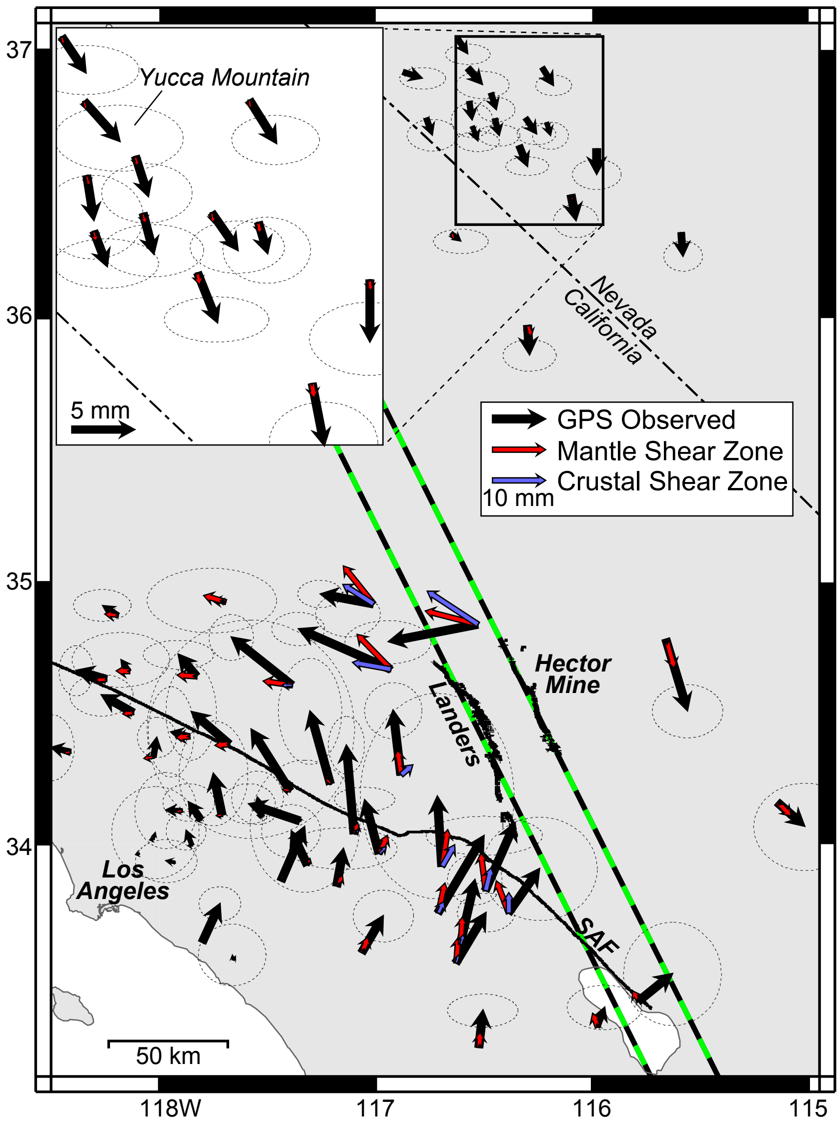

Supplementary Figure S5. Cumulative GPS observed postseismic horizontal surface displacements (transient component) for the 7 year period following the 1999 Hector Mine earthquake compared to those calculated by models of complete relaxation within narrow shear zones below the rupture surfaces and extending hundreds of kilometers to the north and south (green/black dashed lines). Stations within 20 km of the Landers and Hector Mine rupture surfaces have been excluded from this comparison. SAF: San Andreas Fault. Inset: Enlargement of Yucca Mountain region. GPS errors are shown at the 95% confidence level. Crustal shear zone is from 20 to 28 km depth. Mantle shear zone is from 28 to 120 km depth.

Supplementary Table S1. Seven year cumulative displacements and associated errors at GPS stations used in this study. * denotes near-field stations not used in model testing.

Long.	Lat.	East (mm)	North (mm)	Err_E (mm)	Err_N (mm)	Station	Long.	Lat.	East (mm)	North (mm)	Err_E (mm)	Err_N (mm)	Station
-116.429	34.594	-5.27	33.72	3.22	1.94	AGMT*	-116.099	36.459	0.94	-4.83	1.72	1.28	JOHN
-114.932	36.319	2.61	-3.49	1.83	1.50	APEX	-116.433	34.267	8.15	27.23	3.94	1.44	LDES*
-117.522	36.050	7.32	-3.77	3.99	1.83	ARGU	-116.209	34.699	-0.17	-31.17	3.72	4.38	LDSW*
-116.630	33.540	5.71	9.54	2.22	1.50	AZRY	-118.139	34.662	-1.55	2.16	3.77	2.11	LINJ
-117.897	34.126	-3.00	0.11	2.38	2.94	AZU1	-116.308	36.746	2.05	-2.94	1.50	0.83	LITT
-116.884	34.264	-1.44	12.20	2.22	2.16	BBRY	-119.104	34.734	-1.61	-0.50	2.33	1.55	LVMS
-116.621	37.040	1.89	-2.83	1.72	0.78	BEAT	-117.437	33.857	4.49	10.37	4.22	5.10	MATH
-117.065	33.578	4.10	7.04	2.33	2.00	BILL	-115.979	36.633	0.00	-4.83	1.89	1.16	MERC
-118.095	33.962	-3.33	-2.33	2.00	3.00	BKMS	-117.318	33.918	-3.00	6.43	2.27	2.05	MLFP
-114.715	33.610	4.22	2.61	2.66	5.16	BLYT	-116.422	32.892	-10.54	1.89	5.66	3.38	MONP
-116.985	33.963	-2.72	10.21	2.33	0.94	BMRY	-117.210	34.231	-3.83	13.70	2.44	4.10	MSOB
-117.012	34.919	-10.04	1.89	1.72	1.05	BSRY	-116.525	33.211	0.78	7.04	2.72	1.28	MVFD
-116.872	36.918	3.61	-1.16	1.77	0.83	BULL	-116.148	34.509	35.89	-22.24	4.27	2.88	NBPS*
-116.451	36.745	0.83	-3.16	1.61	0.83	BUST	-115.918	34.370	35.28	-11.20	4.10	2.00	OPBL*
-118.026	34.333	0.61	3.72	1.50	1.55	CHIL	-116.305	34.428	30.45	31.61	5.05	2.22	OPCL*
-116.766	36.746	1.11	-3.16	1.94	1.22	CHLO	-116.083	34.367	38.27	4.94	4.38	1.66	OPCP*
-117.828	34.641	-3.44	4.16	2.72	1.11	CHMS	-116.149	34.430	30.01	1.94	3.38	1.66	OPCX*
-116.666	31.871	4.33	2.33	2.55	1.77	CIC1	-116.292	34.533	8.87	17.42	2.11	1.44	OPRD*
-117.709	34.110	-1.66	7.93	2.66	4.05	CLAR	-117.695	34.925	-2.55	0.33	4.99	2.50	PHLB
-118.411	34.353	-3.61	0.83	1.77	2.55	CMP9	-117.243	32.665	13.42	-11.37	3.99	4.55	PLO3
-116.387	33.733	5.88	8.38	4.44	3.99	COTD	-117.182	33.836	1.28	7.15	4.16	1.61	PPBF
-116.569	36.808	0.55	-3.49	1.61	1.33	CRAT	-116.494	33.819	5.66	12.87	1.94	1.33	PSAP
-117.100	34.039	-1.44	16.75	1.39	2.22	CRFP	-117.807	34.092	-2.33	3.33	2.00	1.44	PSDM
-115.735	33.070	-0.72	0.22	5.16	4.33	CRRS	-118.245	34.629	-5.66	1.72	1.33	1.94	QHTP
-116.370	34.124	5.66	19.97	4.05	1.28	CTMS*	-116.625	34.644	-20.58	11.65	2.50	1.72	RDMT*
-115.788	33.390	6.49	5.27	3.77	3.99	DHLG	-116.554	36.715	1.05	-2.77	1.66	0.78	RELA
-116.712	33.733	8.71	14.64	4.49	1.50	DSSC	-116.468	36.840	1.00	-3.11	1.44	0.94	REPO
-117.860	34.413	-3.49	0.83	1.77	3.49	DVPB	-118.026	34.019	0.33	1.22	3.38	3.55	RHCL
-117.526	34.104	-0.83	3.61	2.00	2.05	EWPP	-116.610	33.611	2.77	12.26	2.11	1.94	ROCH
-118.894	34.410	0.00	-5.88	2.83	6.38	FMTP	-117.085	36.218	2.33	-3.49	3.27	2.61	ROGE
-117.398	34.204	-7.32	11.65	7.99	8.43	GHRP	-118.193	34.875	-2.88	1.89	2.22	1.22	RSTP
-115.660	34.784	4.10	-13.59	2.72	2.05	GMRC	-117.353	34.089	-9.60	3.22	2.05	1.55	RTHS
-116.430	34.755	-22.85	-4.88	2.61	2.38	HCMN*	-116.650	36.316	1.77	-1.44	2.11	0.94	RYAN
-115.032	32.706	3.77	-8.43	5.55	6.05	IID2	-117.661	33.553	-0.11	0.89	2.61	2.38	SBCC
-115.145	34.158	5.21	-4.55	3.94	3.38	IMPS	-117.388	34.607	-11.43	9.10	1.72	1.77	SCIA

Supplementary Table 1 (cont).

Long.	Lat.	East (mm)	North (mm)	Err_E (mm)	Err_N (mm)	Station
-116.696	33.913	-0.83	13.31	5.93	7.93	SGPS
-116.299	35.971	0.39	-5.60	2.05	1.22	SHOS
-117.250	32.865	2.00	13.87	5.99	9.76	SIO3
-116.211	36.730	0.72	-2.44	1.39	1.05	SKUL
-115.978	33.292	1.39	3.72	2.88	1.72	SLMS
-115.588	36.320	0.33	-4.44	1.50	1.16	SMYC
-117.929	33.927	-1.61	0.33	2.38	1.66	SNHS
-117.849	33.993	-1.11	2.83	1.55	1.50	SPMS
-115.466	31.045	3.33	1.00	7.15	4.10	SPMX
-116.338	36.645	1.55	-3.88	1.66	0.72	STRI
-117.678	34.382	-7.15	6.16	1.94	3.72	TABL
-116.574	36.932	2.77	-3.11	2.05	1.05	TATE
-116.230	36.935	2.11	-3.38	1.39	0.78	TIVA
-117.803	33.618	3.38	7.38	1.61	1.33	TRAK
-116.530	34.839	-16.92	-3.27	3.33	1.66	TROY
-116.085	33.030	8.10	-0.67	5.32	4.10	USGC
-118.121	34.502	-5.99	3.38	2.44	1.61	VNPS
-116.932	34.669	-17.42	7.65	2.05	1.28	WOMT